

Journal of Materials Chemistry A

Accepted Manuscript



This is an *Accepted Manuscript*, which has been through the Royal Society of Chemistry peer review process and has been accepted for publication.

Accepted Manuscripts are published online shortly after acceptance, before technical editing, formatting and proof reading. Using this free service, authors can make their results available to the community, in citable form, before we publish the edited article. We will replace this *Accepted Manuscript* with the edited and formatted *Advance Article* as soon as it is available.

You can find more information about *Accepted Manuscripts* in the [Information for Authors](#).

Please note that technical editing may introduce minor changes to the text and/or graphics, which may alter content. The journal's standard [Terms & Conditions](#) and the [Ethical guidelines](#) still apply. In no event shall the Royal Society of Chemistry be held responsible for any errors or omissions in this *Accepted Manuscript* or any consequences arising from the use of any information it contains.

Cite this: DOI: 10.1039/c0xx00000x

www.rsc.org/xxxxxx

ARTICLE TYPE

Magnéli Phase Ti_8O_{15} Nanowires as Conductive Carbon-Free Energy Materials to Enhance the Electrochemical Activity of Palladium Nanoparticles for Direct Ethanol Oxidation

Pei Kang Shen^{*a,b}, Chunyong He^c, Shiyong Chang^d, Xiangdong Huang^d, Zhiqun Tian^a

Received (in XXX, XXX) Xth XXXXXXXXX 20XX, Accepted Xth XXXXXXXXX 20XX

DOI: 10.1039/b000000x

Pure single-crystalline magnéli phase Ti_8O_{15} nanowires (NWs) has been successfully synthesized *via* a facile one-step evaporation-deposition synthesis method in hydrogen atmosphere. The electrical conductivity of a single Ti_8O_{15} nanowire is 2060 S m^{-1} at 300 K, which is much higher than carbon black ($\sim 100 \text{ S m}^{-1}$) and almost as high as graphite ($\sim 1000 \text{ S m}^{-1}$) or graphene ($\sim 2000 \text{ S m}^{-1}$). Pd nanoparticles (NPs) loaded on Ti_8O_{15} nanowires are synthesized through a pulsed electrodeposition method. As carbon-free support materials for Pd NPs, the Pd/ Ti_8O_{15} NWs shows a significant enhanced activity for ethanol oxidation reaction and excellent durability compared to Pd/C catalyst. The peak current density of the Pd/ Ti_8O_{15} NWs after 2,000 cycles is $2791 \text{ mA mg}^{-1}_{\text{Pd}}$, only 18.6 % lost. While, on the Pd/C electrode, only a current density of $682 \text{ mA mg}^{-1}_{\text{Pd}}$ is observed, lost 42.3 % of the initial ethanol oxidation reaction activity. The synthetic approach of pure single-crystalline magnéli phase Ti_8O_{15} nanowires gives the inspiration of the development of conductive carbon-free material for electrocatalysis in direct alcohol fuel cells (DAFCs).

Introduction

TiO_2 shows promising applications in environmental remediation, solar energy conversion and other electrochemical energy storage devices¹⁻⁵ since it is no light corrosion, good acidic and alkaline resistance, stable chemical properties, biologically non-toxic and abundant source. Therefore, the synthesis of TiO_2 has attracted significant attention in the past decade. However, TiO_2 is a type of wide band-gap semiconductor, it only adsorbs ultraviolet light, leading to low solar photovoltaic conversion efficiency, which greatly limits its practical applications in solar energy conversion.⁶ In addition, TiO_2 also suffers a realization handicap in the applications of the electrochemical energy storage devices, mainly due to its low electrical conductivity. Narrow the band gap of TiO_2 to extend electronic properties, which is so-called band-gap engineering, is the effective approach to improve its inherent shortcomings. Doping with metal or non-metal elements in TiO_2 is known as a feasible approach to tune the electronic structure of TiO_2 , which leads to new states of TiO_2 for visible light response and performance improvements in electrochemical energy storage.⁷⁻¹⁰ The other efficient approach is introduce oxygen vacancies or Ti^{3+} in TiO_2 to form reduced TiO_2 , black TiO_2 or Magnéli phase $\text{Ti}_n\text{O}_{2n-1}$ ($3 \leq n \leq 10$). These materials can tune the electronic structure of TiO_2 as well and introduce new states into the TiO_2 band gap. Therefore, these materials have been generally used as visible light-absorptive catalysts, or catalyst support and battery electrode materials owing to their high electrical conductivity and unique composition and structures.¹¹⁻¹⁵

Although the fabrication of shape-controlled TiO_2 nano-architectures has been studied extensively, the synthesis of shape-controlled Magnéli phase $\text{Ti}_n\text{O}_{2n-1}$ nano-architectures is

still a great challenge. Traditionally, the Magnéli phase Ti_8O_{15} is synthesized by the thermal reduction of TiO_2 powders at high temperature with H_2 gas or other reductants.¹⁶⁻¹⁸ However, this two-step synthesis strategy inevitably leads to the agglomeration of nanoparticles.¹⁹ Although there have been some reports on the successful synthesis of black TiO_2 nanowires²⁰ or nanotubes²¹ *via* hydrogenation, but the direct synthesis of shape-controlled Magnéli phase $\text{Ti}_n\text{O}_{2n-1}$ nano-architectures by one step is still a big challenge.

Direct alcohol fuel cells (DAFCs), which have been attracting enormous research interest, are considered to be one of the most promising devices for stationary and portable electronic applications owing to their high energy density, fuel portability, and low operating temperature.²²⁻²⁴ Carbon-supported Pt or Pd based catalysts have been studied and applied as electrocatalysts in DAFCs.²⁵⁻²⁷ However, due to the electrochemical corrosion of the carbon supporting material, the durability of carbon-supported catalysts is not able to meet the requirements for commercialized electrocatalyst in DAFCs.²⁸ Accordingly, persistent efforts have been made on the exploration of carbon-free supporting materials in the past decades, including nitride,²⁹ carbide,³⁰ hollow-silica-spheres,³¹ and as well as metal oxides.^{32,33} Owing to the superb electrochemical durability, TiO_2 has been considered as potential support of the precious metal nanoparticles.^{34,35} However, its intrinsic low electrical conductivity greatly restricts its applications.

Herein, we present a facile one-step evaporation-deposition route to pure single-crystalline magnéli phase Ti_8O_{15} NWs as conductive carbon-free support materials for Pd NPs as efficient electrocatalyst in DAFCs. The simple strategy leads to big inspiration for synthesizing conductive shape-controlled transition metal oxides and utilizing them as active and low-cost

catalysts or catalyst supports in electrochemical energy storage devices. The Pd/Ti₈O₁₅ NWs showed significantly enhanced electrocatalytic performance and outstanding durability for ethanol oxidation.

Experimental

Synthesis of Ti₈O₁₅ nanowires.

Experimentally, the Ti₈O₁₅ NWs were grown on Ti foil (Grade 1, purity 99.5%) substrate, the size of Ti foil substrate was 2.5cm×3.0cm×0.5mm (width×length×thickness). Before evaporation-deposition, the Ti foil was chemically polished with HF:HNO₃:H₂O (1:3:6) solution for 5 s to remove the surface impurities and then ultrasonically cleaned in acetone, ethanol and deionized water for 10 min, respectively. Put pure TiO₂ powders (99.0%, 5-10 nm, 2 g) into a quartz boat and placed the quartz boat at the center of a conventional tube furnace (high temperature region, H.T.), while the Ti substrate was located downstream, 6 cm from the quartz boat (low temperature region, L.T.). Before the injection of H₂, the reaction system was flushed with N₂ (50 ml min⁻¹) for 1 h to remove residual oxygen and moisture, then, inflated the tube with H₂ (20 ml min⁻¹) for 30 min. And subsequently, the furnace was heated to 1050 °C at a rate of 8 °C min⁻¹ and kept for 2 h with hydrogen gas flow rate 20 ml min⁻¹. Finally, the furnace was cooled at a rate of 5 °C min⁻¹ down to room temperature, a layer of black material was observed on the surface of the Ti substrate (inset in Fig. 2a).

Preparation of Pd/Ti₈O₁₅ NWs electrocatalysts.

The Pd/Ti₈O₁₅ NWs electrocatalyst was synthesized by pulsed electrodeposition of Pd NPs on Ti₈O₁₅ NWs (acted as working electrode), which was carried out in a thermostat-controlled standard three-electrode electrochemical cell using a computerized potentiostat (Bio-logic VMP3, France). A saturated calomel electrode (SCE) was acted as the reference electrode, a piece of platinum plate electrode (1×1 cm²) as the counter electrode. For the electrodeposition of Pd, 3 mmol L⁻¹ Na₂PdCl₄ was formulated in 0.5 M H₂SO₄ as precursors. The deposition electrolyte was saturated with argon gas during the deposition processes with magnetic stirring. The potential imposed on the electrode was -1.6 V for 0.1 s (pulse nucleation) and a pulse of -0.2 V, corresponding to the nuclei growth for periods of 500 s. Subsequently, the Pd/Ti₈O₁₅ NWs was thoroughly rinsed with deionized water for several times.

Preparation of Pd/C electrocatalysts.

The Pd/C catalyst was prepared *via* adsorption/reduction by IMH method described as follows. The palladium(II) sodium chloride precursor (7.2 ml, 9.2 mg_{Pd} ml⁻¹) was well mixed with ethylene glycol (EG, 50 ml) in an ultrasonic bath. Then, the VC-72 (100 mg) was added into the mixture. The pH of the mixture was adjusted to 10 by 0.1 mol L⁻¹ NaOH/EG solution. After agitation and ultrasonication for 30 min, the mixture was microwave-heated in the process of 5 s-on/5 s-off for 20 times. The resulting black solid sample was acidified, filtered, washed and dried at 80 °C for 12 h in a vacuum oven.

Materials Characterizations.

X-ray diffraction (XRD) analysis was carried out on a D8 ADVANCE powder X-ray diffractometer (Cu K α , 30 kV, 30 mA). Scanning electron microscope (SEM) were performed on thermal field emission environmental SEM-ED-EBS (Quanta

400F, FEI, Oxford, HKL Ltd.). The high-resolution transmission electron microscope (HRTEM) and high-angle annular dark-field scanning transmission electron microscopy-energy dispersive spectroscopy HAADF-STEM-EDS elements mapping were performed using a Tecnai G2 F30 (FEI) operating at 300 kV. The X-ray photoelectron spectroscopy (XPS) measurements were carried out on a XPS apparatus (ESCALAB 250, Thermo-VG Scientific Ltd.). The loadings of Pd were measured by an inductively coupled plasma-atomic emission spectrometry (ICP-AES (IRIS(HR), USA). X-band electron paramagnetic resonance (EPR) spectra of the samples were collected at liquid nitrogen temperature using an electron paramagnetic resonance spectrometer (A300-10-12, BRÜCKNER).

To measure the conductivity under conditions of low energy and bias voltages, a voltage ramp of 0–0.05 V was applied across split electrodes in steps of 0.025 V for two-probe measurements using a source meter (Keithley 2400).

Electrochemical measurements.

The electrocatalytic properties of Pd/Ti₈O₁₅ NWs, represented by the catalytic oxidation of ethanol in DAFCs, were probed on an Bio-logic VMP3 electrochemical workstation in a thermostat-controlled standard three-electrode cell at 30 °C with a Hg/HgO (1.0 mol L⁻¹ KOH) electrode as the reference electrode, a platinum foil (1.0×1.0 cm²) as the counter electrode. The ethanol oxidation reaction on the Pd/Ti₈O₁₅ NWs electrocatalyst was carried out in an nitrogen-saturated 1.0 mol L⁻¹ KOH +1.0 mol L⁻¹ CH₃CH₂OH solution. The cyclic voltammograms (CVs) were recorded at the scan rate of 20 mV s⁻¹ within the potential window of -0.96 to 0.24 V *vs.* Hg/HgO. The durability of the Pd/Ti₈O₁₅ NWs for MOR was measured by performing CVs of Pd/Ti₈O₁₅ NWs over 2,000 cycles using the scan rate of 0.1 V s⁻¹ from -0.96 V to 0.24 V.

Platinum on carbon catalyst (46.7 wt%Pt from TKK, Japan) was also measured for comparison. The catalyst ink was prepared as follows. 5.0 mg catalysts (Pd/C or Pt/C) and 0.5 mL Nafion solution (0.05 wt %, DuPont, USA) solution were dispersed in 0.5 ml of ethanol by sonication for an hour to form a well-dispersed ink. A certain amount of the ink was transferred onto the surface of the glassy carbon electrode. After dried under infrared lamp for 5 min, a catalyst thin film was obtained.

The measured loadings of Pd on Pd/Ti₈O₁₅ NWs electrode were 0.078 mg cm⁻². And we kept the same metal loading on Pd/C and Pt/C electrodes.

Results and Discussions

The product on the Ti substrate was collected and characterized by XRD. For comparison, the anatase TiO₂, rutile TiO₂ powders and Ti substrate were also characterized as shown in Fig. 1a. The diffraction pattern of the product reveals single phase of Ti₈O₁₅. Fig. 1b enlarges the XRD pattern of the product in the 2 θ range from 25° to 45°. The identified peaks in spectrum are indexed as triclinic Ti₈O₁₅ (JCPDF, No. 50-0790).

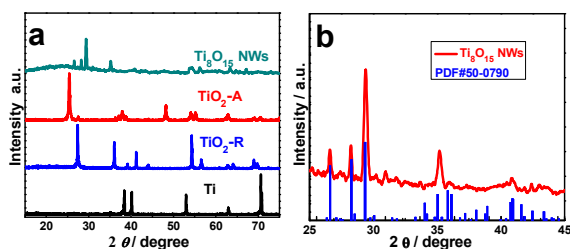


Fig. 1 (a) XRD pattern collected from the Ti_8O_{15} NWs product, anatase TiO_2 ($\text{TiO}_2\text{-A}$), rutile TiO_2 ($\text{TiO}_2\text{-R}$) and Ti substrate and (b) enlarged XRD pattern of Ti_8O_{15} , the blue vertical lines indicate the peaks of the pure Ti_8O_{15} reflections (JCPDF, No. 50-0790).

Fig. 2 demonstrated the morphology and structure of the as-prepared Ti_8O_{15} NWs. Fig. 2a shows the typical plane-view SEM image of the Ti_8O_{15} NWs on Ti substrate. The inset in Fig. 2a is a digital photo of the sample, it revealed that a black layer was grown on the surface of the Ti substrate. Fig. 2b and 2c show the high magnification SEM images of the Ti_8O_{15} NWs, indicating the highly uniform and densely packed array of the nanowires. It reveals an interconnected network, forming a highly hierarchically porous surface morphology. We also investigated the structures of the Ti_8O_{15} NWs with HRTEM and selected area electron diffraction (SAED). Fig. 2d and 2e display the representative low-resolution TEM images of Ti_8O_{15} NWs. The size of individual Ti_8O_{15} NWs was approximately 30 nm in diameter. The typical SEAD pattern in Fig. 2e (inset at top right corner) was taken on a typical individual nanowire (marked by the red circle at the head of the nanowire), the regularly arranged spots showing that the nanosheet is single crystal in nature. The pure Ti_8O_{15} NWs were highly crystallized, as seen from the well-resolved lattice features shown in the HRTEM image (Fig. 2f). Two lattice plane distances of 0.315 nm and 0.281 nm can be clearly seen, corresponding to the $[\bar{1}2\bar{1}]$ and $[1\bar{2}7]$ planes of Ti_8O_{15} .

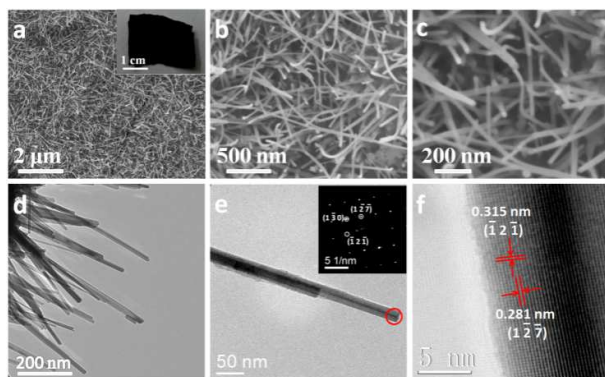


Fig. 2 Morphology and structure of the Ti_8O_{15} NWs. (a) typical SEM image of the Ti_8O_{15} NWs on Ti substrate, the inset in (a) is the digital image of the product, (b,c) high magnification SEM images of the Ti_8O_{15} NWs, (d,e) TEM images of the Ti_8O_{15} NWs, inset in (e) is the corresponding selected area electron diffraction (SAED), (f) HRTEM image of Ti_8O_{15} NWs.

High-angle annular dark-field scanning transmission electron microscopy (HAADF-STEM) analysis and X-ray elemental analysis was carried out to further analyze the structure and investigate the composition of Ti_8O_{15} NWs, as shown in Fig. S1.

Fig. S1a shows the HAADF-STEM image of a typical individual Ti_8O_{15} nanowire, which clearly corroborates the TEM images. The distribution of elements in Ti_8O_{15} NWs was observed using the HAADF-STEM-EDS maps (dotted box in Fig. S1a). Ti and O are uniformly distributed in the Ti_8O_{15} NWs. A line-profile analysis using HAADF-STEM-EDS was applied to analyze the chemical microstructure of the Ti_8O_{15} NWs (Fig. S1d), which is in accordance with the TEM results. Fig. S1e displays the EDS pattern of Ti_8O_{15} NWs.

In order to elucidate the chemical bonding on the Ti_8O_{15} NWs and the absence of Ti^{3+} , we have further carried out X-ray photoelectron spectroscopy (XPS) (Fig. S2). The comparison of the Ti-2p XPS spectra of Ti_8O_{15} NWs and TiO_2 (Fig. S2a) shows that the Ti_8O_{15} NWs and TiO_2 have different features. The TiO_2 shows typical Ti^{4+} features with Ti 2p_{3/2} peak centered at 458.6 eV and Ti 2p_{1/2} peak centered at 464.4 eV.^{36, 37} While Ti_8O_{15} NWs display two additional small shoulder peaks centered at 463.7 and 458.0 eV, which are the characteristic feature of Ti-2p_{1/2} and Ti-2p_{3/2} peaks for the Ti^{3+} ions.³⁸ The O_{1s} core-level XPS spectra show that both of the Ti_8O_{15} NWs and TiO_2 have similar O_{1s} peaks centered at 530.1 eV, which is related to the Ti-O-Ti (Fig. S2b).³⁹ An additional peak at 532.0 eV in Ti_8O_{15} NWs is assigned to Ti-OH bond, which is attributed to the hydrogen atmosphere.⁴⁰ Electron paramagnetic resonance (EPR) spectroscopy, as shown in Fig. 3, sheds more light on the electronic structure of Ti_8O_{15} NWs and TiO_2 . TiO_2 do not show any active ESR signal, suggesting them to be free of $\text{O}_2\cdot$ radicals or Ti^{3+} species. While Ti_8O_{15} NWs display an EPR resonance at $g = 1.98$, indicative of surface Ti^{3+} .⁴¹ This spectral assignment is in accord with our XPS data: some Ti^{3+} is presented in Ti_8O_{15} NWs while only Ti^{4+} in TiO_2 .

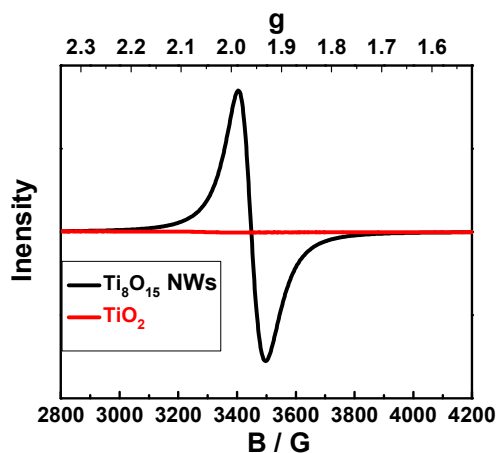


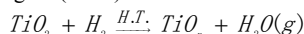
Fig. 3 Comparison of EPR spectra of TiO_2 and Ti_8O_{15} NWs.

Fig. S3 presents the current–voltage (I–V) characteristics of one Ti_8O_{15} nanowires. Inset in Fig. S3 is the schematic diagram of the conductivity measuring experiment. For the two-probe measurement, the linearity of the I–V characteristics was maintained by applying an appropriate low voltage/current. The dissipative power was kept under 1×10^{26} W to eliminate self-heating effects. The electrical conductivity of a single Ti_8O_{15} nanowire was 2060 S m^{-1} at 300 K under calculation.

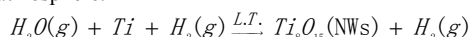
Since the Ti_8O_{15} NWs grown under H_2 atmosphere in the absence of catalyst, the growth mechanism of Ti_8O_{15} NWs cannot be dominated by the vapor-liquid-solid (VLS) mechanism, which is frequently employed to explain the growth of nanowires and nanoarchitectures.^{42, 43} With this in mind, we propose a modified vapor-solid (VS) mechanism to illustrate the growth mechanism

of Ti_8O_{15} NWs.⁴⁴ In a typical VS process, the gas phase reactants were transfer from the high temperature region to low temperature region and directly deposited on the substrate to form nanowires at the low temperature region.⁴⁵ The growth process of the Magnéli phase Ti_8O_{15} nanowires is presented in Scheme 1b. The pre-treatment of the Ti foil substrate lead to a layer of titanium oxide film (the left SEM image in Scheme 1c). When the temperature increases to 1050 °C, a two-step pathway reaction process was proposed in our synthesis process of Ti_8O_{15} NWs, showing as follows.

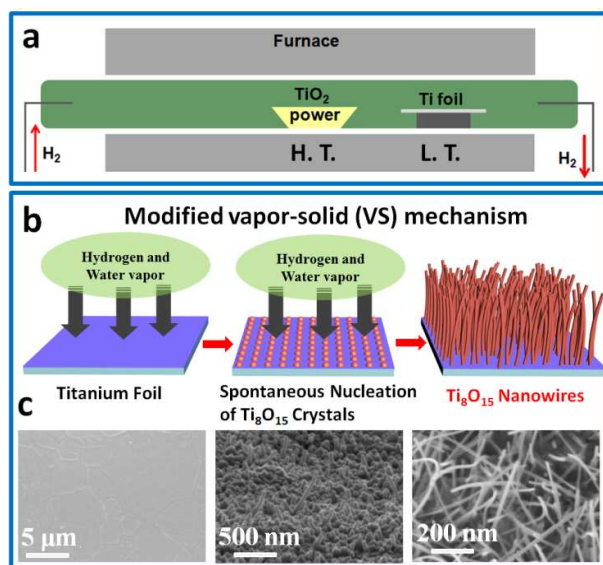
(1) The TiO_2 powders in the quartz boat at the high temperature region (H. T.) were reduced to form H_2O (g);



(2) The H_2O (g) reacted with the Ti on the Ti substrate (the low temperature region, L.T.) to form oxygen-deficient pure single-crystalline Magnéli phase e of Ti_8O_{15} NWs in H_2 atmosphere.



In the nucleation stage of growth of the Ti_8O_{15} NWs, a layer of compact Ti_8O_{15} club-shaped nanoparticles was formed on the Ti foil substrate (the middle SEM image Scheme 1c). In the stage for heat treatment, as time goes on and continuous supply of reactants, the crystal nucleus continue to grow to Ti_8O_{15} NWs (the right SEM image in Scheme 1c).



Scheme 1 (a) Schematic diagram of the experimental apparatus for growth of Ti_8O_{15} NWs, the temperature decreases gradually from centre to the right, giving two temperature regions: high (H.T.) and low temperature (L.T.), (b) schematic illustration of the modified VS process for Ti_8O_{15} NWs growth and (c) corresponding SEM images of the Ti substrate in three different stages.

The Magnéli phase Ti_8O_{15} nanowires were used as carbon-free support to prepare Pd-based electrocatalyst ($\text{Pd}/\text{Ti}_8\text{O}_{15}$ NWs) by a pulsed electrodeposition method. Fig. S4 displays the XRD pattern of $\text{Pd}/\text{Ti}_8\text{O}_{15}$ NWs, showing the Pd and Ti_8O_{15} phases unambiguously. As shown in Fig. S4, the peaks at 40°, 46°, 68° and 81° are assigned to the diffraction of the (111), (200), (220) and (311) crystal planes of the face centered cubic (fcc) structured Pd (JCPDS No. 46-1043), respectively. The other peaks between 25° and 37.0° correspond to the diffraction of Ti_8O_{15} .

Fig. 4a shows a typical bright-field TEM image of the Pd NPs deposited on Ti_8O_{15} NWs. The Pd NPs demonstrate porous interconnected morphology of relatively uniform size distribution and good dispersion on the Ti_8O_{15} NWs surface. The lattice fringes of the Ti_8O_{15} (105) plane and Pt (111) plane indexed in Fig. 4b and 4c, respectively, indicating the formation of polycrystalline Pd NPs on the Ti_8O_{15} NWs surface. These TEM images reveal that the Pd NPs (average size of ~3.5 nm) interconnected and adhered to the Ti_8O_{15} NWs surface (Fig. 4g), producing a polycrystalline Pd structure. Fig. 4d shows the HAADF-STEM image of $\text{Pd}/\text{Ti}_8\text{O}_{15}$ NWs, confirming the porous interconnected morphology of $\text{Pd}/\text{Ti}_8\text{O}_{15}$ NWs. The elemental mapping analysis of Ti and Pd using HAADF-STEM-EDS, obtained from the red box in the Fig. 4d, reveals the uniform distribution of the Ti and Pd components in the nanocomposite (Fig. 4e and 4f), confirming the results of the HRTEM and HAADF-STEM analysis. Fig. 4h presents the EDS pattern of $\text{Pd}/\text{Ti}_8\text{O}_{15}$ NWs, the co-existence of Ti, O and Pd further confirms the above results.

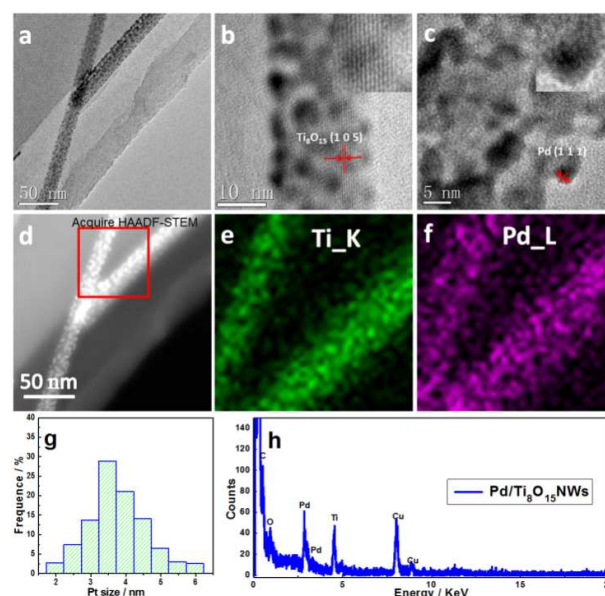


Fig. 4 Morphology and structure of the $\text{Pd}/\text{Ti}_8\text{O}_{15}$ NWs. (a) TEM image of $\text{Pd}/\text{Ti}_8\text{O}_{15}$ NWs, (b,c) HRTEM images of $\text{Pd}/\text{Ti}_8\text{O}_{15}$ NWs, insets are the corresponding enlarged images, (d) HAADF-STEM image of $\text{Pd}/\text{Ti}_8\text{O}_{15}$ NWs, the corresponding elemental mapping for titanium (e) and palladium (f) in $\text{Pd}/\text{Ti}_8\text{O}_{15}$ NWs obtained from the red box in (d), (g) the corresponding size-distribution histograms of the Pd NPs and (h) EDS pattern of $\text{Pd}/\text{Ti}_8\text{O}_{15}$ NWs.

The catalytic properties of the as-prepared $\text{Pd}/\text{Ti}_8\text{O}_{15}$ NWs were investigated for direct ethanol oxidation reaction. For comparison, the ethanol oxidation reaction activities of Pd/C and Pt/C were also investigated in the same conditions. The cyclic voltammograms (CVs) of the Pd/C, $\text{Pd}/\text{Ti}_8\text{O}_{15}$ NWs and Pt/C in N_2 -saturated 1.0 mol L^{-1} KOH with the scan rate of 20 mV s^{-1} at 30 °C were recorded as shown in Fig. 5a. The $\text{Pd}/\text{Ti}_8\text{O}_{15}$ NWs appear to have similar columbic features compared to the Pd/C. Three potential peaks were observed in the anodic scan, which correspond to different electrochemical processes occurring over the Pd surface: 1) the peak (Region A) that appeared at potentials lower than -0.75 V is associated with the oxidation of adsorbed and desorbed hydrogen ($\text{Pd} - \text{H}_{\text{abs/ads}} + \text{OH}^- \rightarrow \text{Pd} + \text{H}_2\text{O} + \text{e}^-$); 2) the peak (Region B) occurs at potentials of ~ -0.4 V and is

related to the adsorption of hydroxyl groups ($\text{Pd} + \text{OH}^- \leftrightarrow \text{Pd} - \text{OH}_{\text{ads}} + e^-$); 3) the peak (Region C) occurs at potentials above -0.2 V can be attributed to the formation of the palladium(II) oxide layer on the surface of the catalyst ($\text{Pd} - \text{OH}_{\text{ads}} + \text{OH}^- \leftrightarrow \text{Pd} - \text{O} + \text{H}_2\text{O} + e^-$).⁴⁶ In the cathodic scan, a peak (Region D) centered at about -0.23 V was observed, which is associated with the reduction of Pd ($\text{Pd} - \text{O} + \text{H}_2\text{O} + 2e^- \leftrightarrow \text{Pd} + 2\text{OH}^-$), Region E correspond to the absorption of hydrogen.

To evaluate the electrocatalytic activity of Pd/Ti₈O₁₅ NWs, the ethanol oxidation reaction has been carried out in 1.0 mol L^{-1} KOH. Fig. 5b compares the CVs recorded for the Pd/C, Pd/Ti₈O₁₅ NWs and Pt/C at 50 mV s^{-1} in 1.0 mol L^{-1} KOH + 1.0 mol L^{-1} CH₃CH₂OH solution. The observed voltammetric curves are excellent signatures of ethanol oxidation at all three electrodes. The Pd/Ti₈O₁₅ NWs showed enhanced electrocatalytic activity compared to Pd/C and Pt/C counterparts: the Pd/Ti₈O₁₅ NWs gave more negative onset potential ($-0.543 \text{ V vs Hg/HgO}$) than that of Pd/C ($-0.451 \text{ V vs Hg/HgO}$) and Pt/C ($-0.490 \text{ V vs Hg/HgO}$) alone with higher peak current densities ($3430 \text{ mA mg}^{-1}_{\text{Pd}}$) compared to Pd/C ($1194 \text{ mA mg}^{-1}_{\text{Pd}}$) and Pt/C ($1853 \text{ mA mg}^{-1}_{\text{Pt}}$). The onset potential (E_{onset}) describes the ease at which electro-oxidation occurs at the catalyst, thus it should be more negative for the best-performing electrocatalysts for ethanol oxidation reaction. The Pd/Ti₈O₁₅ NWs exhibits a 2.9- and 1.8-fold enhancement in mass activity compared to the Pd/C and Pt/C, respectively. Given the above, the Pd/WC_p/G catalyst exhibits the best electro-oxidation activity toward ethanol among the three catalysts. The reaction activation free energy (ΔG°) is related to the activities of the catalysts. A lower ΔG° corresponds to a higher activity. The lower ΔG° value of 24.6 J mol^{-1} was obtained for the ethanol oxidation on Pd/Ti₈O₁₅ NWs as compared to 35.2 J mol^{-1} on Pd/C, indicating improved kinetics (Fig. S5).

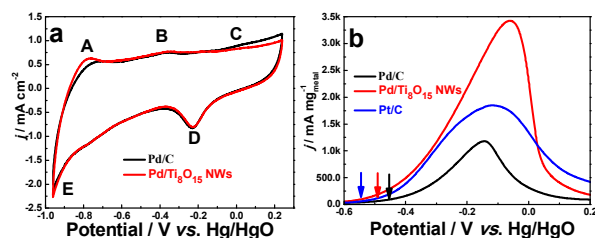


Fig. 5 (a) Typical cyclic voltammograms (CVs) of Pd/C and Pd/Ti₈O₁₅ NWs in N_2 -saturated 1.0 mol L^{-1} KOH with the scan rate of 20 mV s^{-1} at 30°C and (b) CVs recorded at 50 mV s^{-1} of Pd/C, Pd/Ti₈O₁₅ NWs and Pt/C in 1.0 mol L^{-1} KOH + 1.0 mol L^{-1} CH₃CH₂OH solution.

The mechanism of ethanol oxidation reaction is complicated as it involves the generation of several intermediate products (such as linearly adsorbed CO, adsorbed CH_x species) and final products (such as CO₂, acetaldehyde and acetic acid).⁴⁷⁻⁴⁹ So one major problem concerning ethanol oxidation on noble metals is the adsorption of poisoning intermediates, which leads to the deactivation of the electrode surface for further oxidation. A steady-state measurement was used to evaluate the level of the electrode surface contamination with adsorbed poisoning carbonaceous species. The respective chronopotentiometric curves for ethanol oxidation on Pd/C, Pd/Ti₈O₁₅ NWs and Pt/C electrodes at current density of 5 mA cm^{-2} are shown in Fig. 6a. The potential oscillation appeared on the Pt/C electrode after 546 seconds of constant current polarization, indicating the

deterioration and poisoning due to the adsorption of poisonous species on the surface of platinum, which need higher potentials to oxidize the adsorbed poisonous species and release a clean surface.^{50,51} The chronopotentiometric curves for ethanol oxidation on Pd/C and Pd/Ti₈O₁₅ NWs are smooth. The potential to satisfy the applied anodic current density on Pd/Ti₈O₁₅ NWs is lower than that of Pd/C and Pt/C, lower potential means higher output voltage and power density, which indicate ethanol oxidation on Pd/Ti₈O₁₅ NWs via a more efficient pathway and no obvious poisonous species on the surfaces of the Pd/Ti₈O₁₅ NWs. The anti-poisoning ability of the catalyst can be characterized by the time (T) that the catalyst can sustain activity for ethanol oxidation at low overpotential. As shown in Fig. 6a, the T values decrease in this order: Pd/Ti₈O₁₅ NWs ($>3000 \text{ s}$) $>$ Pd/C (2300 s) $>$ Pt/C (1711 s). The above results prove that the Pd/Ti₈O₁₅ NWs catalyst exhibits better electrocatalytic properties and better resistance to poisoning than the Pd/C and Pt/C catalysts. The application of traditional carbon-supported Pd-based catalysts in DAFCs is not only hindered by the electrochemical corrosion of the carbon supporting material, but also suffered by the deactivation of Pd NPs. The deactivation mechanism of the Pd-based catalysts in the process of DAFCs operation is that gradual build-up of adsorbed poisonous species on the surfaces of the Pd block the catalytic active sites.⁵²

The stability of the electrocatalysts under continuous operating conditions was further examined by chronoamperometric measurements. As shown in Fig. 6b, the chronoamperometry (CA) profiles for ethanol oxidation on Pd/C, Pd/Ti₈O₁₅ NWs and Pt/C at a potential of -0.15 V (vs Hg/HgO) for 1600 s in 1.0 mol L^{-1} KOH + 1.0 mol L^{-1} CH₃CH₂OH solution. As displayed in Fig. 6b, initial rapid decreases in current density were observed for Pd/C and Pt/C electrodes, which could be ascribed to the accumulation of strongly adsorbed poisonous reaction intermediates on the surface active sites.⁵³ While on the Pd/Ti₈O₁₅ NWs electrode, the initial descent of current density is slow, which indicates that the deactivation caused by the adsorbed poisonous reaction intermediates on the Pd/Ti₈O₁₅ NWs electrode is much lighter than that on Pd/C and Pt/C, which is consistent with the previous analysis. From Fig. 6b, we conclude that the activity order of ethanol oxidation reaction in term of the current density is Pd/Ti₈O₁₅ NWs $>$ Pt/C $>$ Pd/C. In particular, the Pd/Ti₈O₁₅ NWs exhibits 8.9- and 4.2-fold enhancement in mass activity compared to Pd/C and Pt/C after 1600 s reaction, respectively.

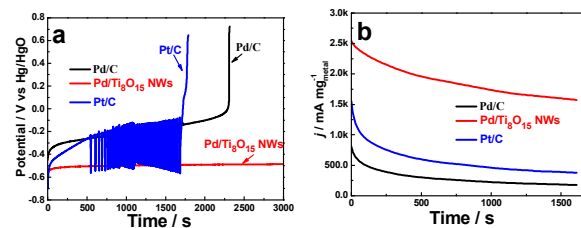


Fig. 6 (a) The chronopotentiometric curves of Pd/C, Pd/Ti₈O₁₅ NWs and Pt/C catalysts at anodic current density of 5 mA cm^{-2} and (b) chronoamperometric curves for the oxidation of ethanol catalyzed by Pd/C, Pd/Ti₈O₁₅ NWs and Pt/C at 0.3 V (vs. SCE) in N_2 -saturated in 1.0 mol L^{-1} KOH + 1.0 mol L^{-1} CH₃CH₂OH solution.

The stability of the electrocatalysts under continuous operating conditions was further examined by continuous potentiodynamic swept between $-0.6 - 0.2 \text{ V}$ (vs. Hg/HgO). Fig. 7a and 7b display the CVs for the ethanol oxidation reaction on Pd/Ti₈O₁₅ and Pd/C

electrodes before and after 2,000 cycles of potentiodynamic swept test. The peak current density of the Pd/Ti₈O₁₅ after 2,000 cycles was 2791 mA mg⁻¹_{Pd}, only an 18.6 % lost. While, on the Pd/C electrode, only a current density of 682 mA mg⁻¹_{Pd} was observed, lost 42.3% of the initial ethanol oxidation reaction activity (Fig. 7c).

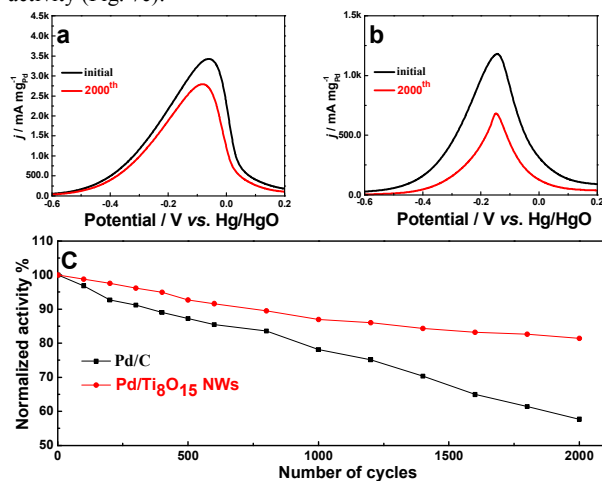


Fig. 7 Polarization curves for the ethanol oxidation reaction on (a) Pd/Ti₈O₁₅ NWs and (b) Pd/C electrodes before and after the continuous CVs cycling test in N₂-saturated in 1.0 mol L⁻¹ KOH + 1.0 mol L⁻¹ CH₃CH₂OH solution and (c) comparison of the peak current density changing with cycle time for the Pd/C and Pd/Ti₈O₁₅ NWs.

Based on above results, the electrocatalytic performance and catalytic stability of Pd/Ti₈O₁₅ NWs electrode for ethanol oxidation reaction in DAFCs are distinctly improved compare with Pd/C. Firstly, oxygen vacancies/Ti³⁺ in Ti₈O₁₅ NWs generate a population of surface electrons available for conduction, and higher electron transfer efficiency can be achieved in the Pd/Ti₈O₁₅ NWs electrode during the catalytic process, which enhance the ethanol oxidation reaction activity and durability.⁵⁴ Moreover, Ti₈O₁₅ NWs can change the hydroxyl/ ethanol adsorption conditions, which is a predominant issue involved in the kinetics of the ethanol oxidation reaction,⁴⁶ through the change of electronic structure of Pd, connected to the electronic interactions between Pd and the supporting material (Ti₈O₁₅ NWs). These interactions are to be expected since Ti₈O₁₅ NWs has hypo-*d*-electron character and could have the ability to interact with Pd that also has hyper-*d*-electron character.^{55,56} This electronic interaction between Pd and Ti₈O₁₅ NWs leads to higher catalytic activity of the OH_{ads} state in the Pd surface, and then facilitates the interaction of Pd-(CH₃CO)_{ads} with Pd-OH_{ads} (Pd-(CH₃CO)_{ads} + Pd-OH_{ads} → Pd-CH₃COOH + Pd), increasing activity of the catalyst for ethanol oxidation reaction.⁵⁷ In order to provide insight into the origin of the promotional effect of Pd/Ti₈O₁₅ NWs, XPS was applied to investigate the electronic structure of Pd in Pd/C and Pd/Ti₈O₁₅ NWs. Fig. 8 shows the comparison of the Pd3d XPS spectra of Pd/C and Pd/Ti₈O₁₅ NWs. Compare to Pd/C, the Pd3d peaks of Pd/Ti₈O₁₅ NWs shift, by about 0.6 eV, to a lower binding energy. The weakened 3d electrons binding energy of Pd in Pd/Ti₈O₁₅ NWs is likely resulted from electronic interaction between the Pd and Ti₈O₁₅ NWs, which through an partial electron transfer from Ti₈O₁₅ NWs to Pd. The electron transfer would increase the electron density of Pd and enhance the penetration of outer-layer electrons to the inner layer, which further down shifts the *d*-band center of

Pd⁵⁸ and substantially enhanced activity toward ethanol oxidation reaction.

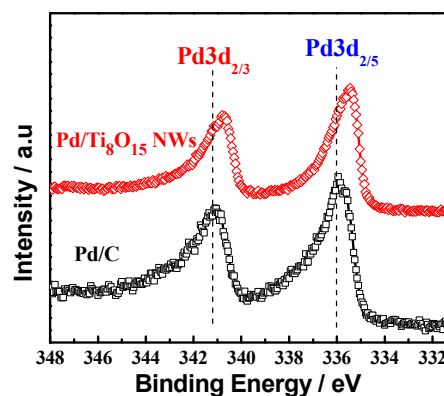


Fig. 8 XPS spectra of the Pd 3d region for Pd/C and Pd/Ti₈O₁₅ NWs.

Conclusions

In conclusion, we have successfully synthesized pure single-crystalline magnéli phase Ti₈O₁₅ NWs through a facile one-step evaporation-deposition synthesis approach. A tentative modified vapor-solid (VS) mechanism was proposed in this work to illustrate the growth mechanism of Ti₈O₁₅ NWs. The electrical conductivity of a single Ti₈O₁₅ nanowire is 2060 S m⁻¹ at 300 K, which is much higher than carbon black (~100 S m⁻¹) and almost as high as graphite (~1000 S m⁻¹) or graphene (~2000 S m⁻¹). Served as conductive carbon-free support material, Ti₈O₁₅ NWs were used to load Pd NPs to form Pd/Ti₈O₁₅ NWs. Compared with Pd/C, the Pd/Ti₈O₁₅ NWs showed a significant enhanced activity for ethanol oxidation reaction and outstanding durability, making it a possible candidate for the next generation electrocatalyst in DAFCs.

Acknowledgements

This work was supported by the Major International (Regional) Joint Research Project (51210002), the National Basic Research Program of China (2015CB932304) and the Guangzhou Automobile Group Project (XW6). PKS acknowledge the support from the Danish project of Initiative toward Non-precious Metal Polymer Fuel Cells (4106-000012B).

Notes and references

- ^a Collaborative Innovation Center of Sustainable Energy Materials, Guangxi University, Nanning, Guangxi, 530004, PR China
- ^b State Key Laboratory of Optoelectronic Materials and Technologies, School of Physics and Engineering, Sun Yat-sen University, Guangzhou, 510275, PR China
- ^c Dongguan Institute of Neutron Science (DINS), and Dongguan Branch, Institute of High Energy Physics, Chinese Academy of Sciences, Dongguan 523800, China

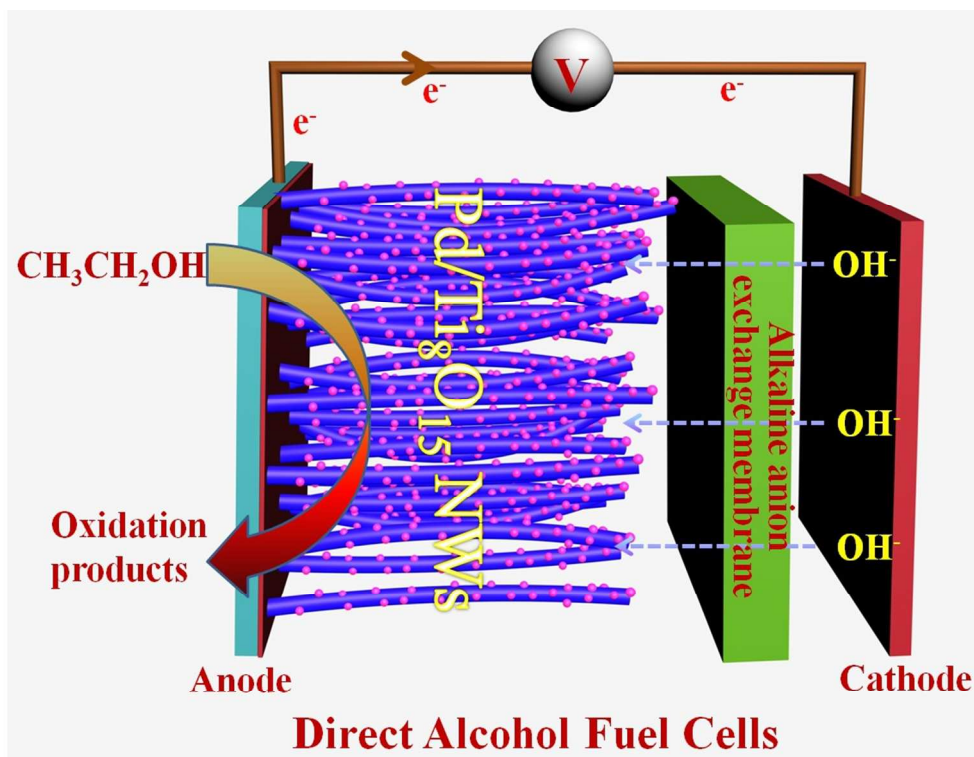
^d *Automotive Engineering Institute, Guangzhou Automobile Group Co., Ltd, Guangzhou, 510640, PR China*

Corresponding Author

* e-mail: pkshen@gxu.edu.cn (P.K. Shen)

- L. Li, J. Yan, T. Wang, Z.-J. Zhao, J. Zhang, J. Gong and N. Guan, *Nat. Commun.*, 2015, **6**, 5881.
- Y. Ma, X. Wang, Y. Jia, X. Chen, H. Han and C. Li, *Chem. Rev.*, 2014, **114**, 9987-10043.
- T. Xia, Y. Zhang, J. Murowchick and X. Chen, *Catal. Today*, 2014, **225**, 2-9.
- S. Su, Z. Huang, Y. NuLi, F. Tuerxun, J. Yang and J. Wang, *Chem. Commun.*, 2015, **51**, 2641-2644.
- K. Jukk, N. Kongi, A. Tarre, A. Rosental, A. B. Treshchalov, J. Kozlova, P. Ritslaid, L. Matisen, V. Sammelselg and K. Tammeveski, *J. Electroanal. Chem.*, 2014, **735**, 68-76.
- X. Chen and S. S. Mao, *Chem. Rev.*, 2007, **107**, 2891-2959.
- R. Asahi, T. Morikawa, T. Ohwaki, K. Aoki and Y. Taga, *Science*, 2001, **293**, 269-271.
- M. Liu, X. Qiu, M. Miyauchi and K. Hashimoto, *J. Am. Chem. Soc.*, 2013, **135**, 10064-10072.
- A. Kumar and V. Ramani, *ACS Catal.*, 2014, **4**, 1516-1525.
- J. Zhang, T. Huang, L. Zhang and A. Yu, *J. Phys. Chem. C*, 2014, **118**, 25300-25309.
- S. Hoang, S. P. Berglund, N. T. Hahn, A. J. Bard and C. B. Mullins, *J. Am. Chem. Soc.*, 2012, **134**, 3659-3662.
- X. Chen, L. Liu, P. Y. Yu and S. S. Mao, *Science*, 2011, **331**, 746-750.
- T. Ioroi, H. Senoh, S.-i. Yamazaki, Z. Siroma, N. Fujiwara and K. Yasuda, *J. Electrochem. Soc.*, 2008, **155**, B321-B326.
- A. Kitada, G. Hasegawa, Y. Kobayashi, K. Miyazaki, T. Abe, K. Kanamori, K. Nakanishi and H. Kageyama, *RSC Advances*, 2013, **3**, 7205-7208.
- C. He, S. Chang, X. Huang, Q. Wang, A. Mei and P. K. Shen, *Nanoscale*, 2015, **7**, 2856-2861.
- C. Acha, M. Monteverde, M. Nñuez-Regueiro, A. Kuhn and M. A. Alario Franco, *Eur. Phys. J. B*, 2003, **34**, 421-428.
- Y. Lu, Y. Matsuda, K. Sagara, L. Hao, T. Otomitsu and H. Yoshida, *Adv. Mater. Res.*, 2011, **415-417**, 1291-1296.
- A. Kitada, G. Hasegawa, Y. Kobayashi, K. Kanamori, K. Nakanishi and H. Kageyama, *J. Am. Chem. Soc.*, 2012, **134**, 10894-10898.
- S. Perera, N. Zelenski and E. G. Gillan, *Chem. Mater.*, 2006, **18**, 2381-2388.
- G. Wang, H. Wang, Y. Ling, Y. Tang, X. Yang, R. C. Fitzmorris, C. Wang, J. Z. Zhang and Y. Li, *Nano Lett.*, 2011, **11**, 3026-3033.
- N. Liu, C. Schneider, D. Freitag, M. Hartmann, U. Venkatesan, J. Müller, E. Spiecker and P. Schmuki, *Nano Lett.*, 2014, **14**, 3309-3313.
- X. Zhao, M. Yin, L. Ma, L. Liang, C. Liu, J. Liao, T. Lu and W. Xing, *Energy Environ. Sci.*, 2011, **4**, 2736-2753.
- Z. Jiang, X. Zhao, Y. Fu and A. Manthiram, *J. Mater. Chem.*, 2012, **22**, 24862-24869.
- M. C. Figueiredo, O. Sorsa, N. Doan, E. Pohjalainen, H. Hildebrand, P. Schmuki, B. P. Wilson and T. Kallio, *J. Power Sources*, 2015, **275**, 341-350.
- S. Sun, G. Zhang, N. Gauquelin, N. Chen, J. Zhou, S. Yang, W. Chen, X. Meng, D. Geng, M. N. Banis, R. Li, S. Ye, S. Knights, G. A. Botton, T.-K. Sham and X. Sun, *Sci. Rep.*, 2013, **3**, 1775.
- C.-H. A. Tsang, K. N. Hui, K. S. Hui and L. Ren, *J. Mater. Chem. A*, 2014, **2**, 17986-17993.
- W. Yuan, Y. Cheng, P. K. Shen, C. M. Li and S. P. Jiang, *J. Mater. Chem. A*, 2015, **3**, 1961-1971.
- Y.-J. Wang, D. P. Wilkinson and J. Zhang, *Chem. Rev.*, 2011, **111**, 7625-7651.
- Y. Xiao, G. Zhan, Z. Fu, Z. Pan, C. Xiao, S. Wu, C. Chen, G. Hu and Z. Wei, *Electrochim. Acta*, 2014, **141**, 279-285.
- M. K. Jeon, H. Daimon, K. R. Lee, A. Nakahara and S. I. Woo, *Electrochem. Commun.*, 2007, **9**, 2692-2695.
- A. A. Melvin, V. S. Joshi, D. C. Poudyal, D. Khushalani and S. K. Haram, *ACS Appl. Mater. Interfaces*, 2015, **7**, 6590-6595.
- B. Abida, L. Chirchi, S. Baranton, T. W. Napporn, H. Kochkar, J.-M. Léger and A. Ghorbel, *Appl. Catal., B: Environ.*, 2011, **106**, 609-615.
- M. S. Ide, D. D. Falcone and R. J. Davis, *Journal of Catalysis*, 2014, **311**, 295-305.
- K.-W. Park and K.-S. Seol, *Electrochem. Commun.*, 2007, **9**, 2256-2260.
- S. J. Yoo, T.-Y. Jeon, K.-S. Lee, K.-W. Park and Y.-E. Sung, *Chem. Commun.*, 2010, **46**, 794-796.
- X. Chen, L. Liu, Y. Y. Peter and S. S. Mao, *Science*, 2011, **331**, 746-750.
- X. Chen and C. Burda, *J. Am. Chem. Soc.*, 2008, **130**, 5018-5019.
- Z. Song, J. Hrbek and R. Osgood, *Nano Lett.*, 2005, **5**, 1327-1332.
- G. Lu, S. L. Bernasek and J. Schwartz, *Surf. Sci.*, 2000, **458**, 80-90.
- X. Lu, G. Wang, T. Zhai, M. Yu, J. Gan, Y. Tong and Y. Li, *Nano Lett.*, 2012, **12**, 1690-1696.
- V. Etacheri, J. E. Yourey and B. M. Bartlett, *ACS Nano*, 2014, **8**, 1491-1499.
- X. Duan and C. M. Lieber, *Adv. Mater.*, 2000, **12**, 298-302.
- Y. Hao, G. Meng, Z. L. Wang, C. Ye and L. Zhang, *Nano Lett.*, 2006, **6**, 1650-1655.
- Z. W. Pan, Z. R. Dai and Z. L. Wang, *Science*, 2001, **291**, 1947-1949.

45. J. Zhou, N. S. Xu, S. Z. Deng, J. Chen, J. C. She and Z. L. Wang, *Adv. Mater.*, 2003, **15**, 1835-1840.
46. Z. X. Liang, T. S. Zhao, J. B. Xu and L. D. Zhu, *Electrochim. Acta*, 2009, **54**, 2203-2208.
47. X. Fang, L. Wang, P. K. Shen, G. Cui and C. Bianchini, *J. Power Sources*, 2010, **195**, 1375-1378.
48. C. Bianchini and P. K. Shen, *Chem. Rev.*, 2009, **109**, 4183-4206.
49. M. B. Rohwer, R. M. Modibedi and K. I. Ozoemena, *Electroanalysis*, 2015, **27**, 1-8.
50. M. Krausa and W. Vielstich, *J. Electroanal. Chem.*, 1995, **399**, 7-12.
51. P. Justin and G. Ranga Rao, *Int. J. Hydrogen Energy*, 2011, **36**, 5875-5884.
52. X. Yu and P. G. Pickup, *Electrochem. Commun.*, 2009, **11**, 2012-2014.
53. W. Du, K. E. Mackenzie, D. F. Milano, N. A. Deskins, D. Su and X. Teng, *ACS Catal.*, 2012, **2**, 287-297.
54. F. Shi, L. R. Baker, A. Hervier, G. A. Somorjai and K. Komvopoulos, *Nano Lett.*, 2013, **13**, 4469-4474.
55. L. M. Vračar, N. V. Krstajić, V. R. Radmilović and M. M. Jakšić, *J. Electroanal. Chem.*, 2006, **587**, 99-107.
56. B. Babić, J. Gulicovski, L. Gajić-Krstajić, N. Elezović, V. R. Radmilović, N. V. Krstajić and L. M. Vračar, *J. Power Sources*, 2009, **193**, 99-106.
57. S. Neophytides, S. Zafeiratos, G. Papakonstantinou, J. Jaksic, F. Paloukis and M. Jaksic, *Int. J. Hydrogen Energy*, 2005, **30**, 393-410.
58. D. J. Ham, C. Pak, G. H. Bae, S. Han, K. Kwon, S.-A. Jin, H. Chang, S. H. Choi and J. S. Lee, *Chem. Commun.*, 2011, **47**, 5792-5794.



Pure single-crystalline magnéli phase Ti_8O_{15} nanowires (NWs) has been successfully synthesized and shows a significant enhanced activity for ethanol oxidation reaction and excellent durability.
308x239mm (96 x 96 DPI)